

Pore-scale Observation of Microsphere Deposition at Grain-to-Grain Contacts over Assemblage-scale Porous Media Domains Using X-ray Microtomography

XIQING LI,[†] CHEN-LUH LIN,[‡]
JAN D. MILLER,[‡] AND
WILLIAM P. JOHNSON*^{·†}

*Department of Geology & Geophysics, University of Utah,
Salt Lake City, Utah 84112 and Department of Metallurgical
Engineering, University of Utah, Salt Lake City, Utah 84112*

The prevalence of colloid deposition at grain-to-grain contacts in two porous media (spherical glass beads and angular quartz sand, 710–850 μm) was examined using X-ray microtomography (XMT) under conditions where the colloid-grain surface interaction was solely attractive (lacking an energy barrier to deposition), and under fluid velocity conditions representative of engineered filtration systems. XMT allows pore-scale observation of colloid deposition over assemblage-scale porous media domains. Colloids visible in reconstructed images were prepared by coating gold on hollow ceramic microspheres (36 μm in size) (to render densities only slightly higher than water). A significant fraction of the deposited microspheres were deposited at grain-to-grain contacts (about 20% in glass beads, 40% in quartz sand) under the conditions examined. The deposited microsphere concentrations decreased log-linearly with increasing transport distance regardless of the environment of deposition (grain-to-grain contact versus single-contact deposition). The profile shape was, therefore, consistent with filtration theory, and the observed deposition rate coefficients were also well predicted by filtration theory. The ability of filtration theory to predict the magnitude and spatial distribution of deposition demonstrates that filtration theory captures the essential elements of deposition in the absence of an energy barrier despite a lack of accounting for grain-to-grain contacts. The observed factor of 2 greater deposition at grain-to-grain contacts in quartz sand relative to equivalently sized glass beads is consistent with greater grain-to-grain contact lengths and greater fraction of small pores in the quartz sand relative to the glass beads, as determined via a pore structure analysis algorithm (medial axis algorithm).

Introduction

Colloid deposition during transport in porous media is commonly described using filtration theory (1–4). The

centerpiece of classic filtration theory is the single collector efficiency (η) which represents the probability of colloid collision with grain surfaces upon approach. The porous media is idealized as an assemblage of individual spherical collectors (grains) that are each completely surrounded by a spherical shell of fluid (2, 5). The idealized uniform fluid envelope is scaled to maintain the porosity of the actual porous media. In reality, the packed porous media structure is built on grain-to-grain contacts, and the fluid envelopes cannot completely cover the grain surfaces, nor be of uniform thickness.

The limited effort, to date, that has been directed toward development of models that account for grain-to-grain contacts has indicated that these features may help to explain well-known shortcomings of classic filtration theory (6), such as the relative insensitivity of observed colloid deposition to solution chemistry changes in the presence of an energy barrier (7). The potential importance of grain-to-grain contacts is also indicated indirectly in re-packed porous media transport experiments, where straining (physical entrapment in pore constrictions) has been suggested to play an important role in colloid deposition (8). Traditionally, straining has been considered insignificant when the ratio of the colloid to collector diameter is less than 0.05 (9, 10). However, Bradford et al. (11) recently suggested that this threshold should be lowered by an order of magnitude (i.e., 0.005).

Experimental verification of the influence of grain-to-grain contacts on colloid deposition has been limited by the inability of existing techniques to yield pore-scale resolution over an assemblage-scale domain. Direct observation of the environment of deposition is not possible in conventional re-packed column transport experiments. Techniques that potentially allow direct observation of the environment of deposition include light microscopy, magnetic resonance imaging (MRI), and X-ray microtomography (XMT). Light microscopy provides pore-scale resolution (e.g., 12–14); however, observation is restricted to very small domains (e.g., a single pore). MRI yields column-scale observation, but lacks pore scale resolution (e.g., <100 μm) (15–17).

In the past two decades, XMT has demonstrated the potential to provide pore-scale resolution over assemblage-scale domains of porous media. XMT involves passing X-rays through the sample from multiple directions and measuring attenuation to derive projections of the sample. From the projections, the image of the sample is obtained using a reconstruction algorithm (e.g., filtered back-projection) (18). Using microfocus X-ray sources or synchrotron radiation, XMT can achieve spatial resolution down to a few μm (19, 20), a resolution sufficient for pore-scale observation. The domain of observation typically ranges from a few to several tens of centimeters (19, 20), depending inversely on the resolution used.

XMT has been used to characterize pore structure (21–28) and multi-fluid phase distribution in porous media (20, 29, 30). XMT images have also been employed to estimate fluid flow and transport properties within a pore domain (21, 25, 26, 31, 32) and to model flow and transport in porous media (23–25, 27, 33–35). To the best of our knowledge, XMT has not been used to directly examine the environment of deposition of colloids in porous media. This is due to the challenge of developing colloids that are sufficiently large to be XMT-visible while maintaining an environmentally relevant density. Colloids must, by definition, be sufficiently small, or of sufficiently low density, to remain suspended in water for significant periods of time. In the environment,

* Corresponding author phone: (801) 581-5033; fax: (801) 581-7065; e-mail: wjohnson@mines.utah.edu.

[†] Department of Geology & Geophysics, University of Utah.

[‡] Department of Metallurgical Engineering, University of Utah.

large colloids (e.g., several μm) are composed of low atomic number elements (e.g., C, H, and O for bacteria or protozoa), which due to their low attenuation coefficients provide insufficient contrast relative to the water and the porous media. Small colloids (e.g., tens of nm or less) may contain high atomic number elements (e.g., Fe). However, these colloids are not visible since their overall mass yields too low attenuation contrast relative to the pore water and porous media.

The objective of the paper is to introduce an XMT strategy using gold-coated hollow ceramic microspheres in direct observation of colloid deposition environments in porous media. We demonstrate that in the absence of an energy barrier, colloid deposition at grain-to-grain contacts is significant, but does not dominate overall deposition, yielding results that are in agreement with classic filtration theory. This paper also sets the stage for a companion paper examining the influence of grain-to-grain contacts on colloid deposition in porous media in the presence of an energy barrier.

Materials and Methods

Preparation of Gold-Coated Hollow Microspheres. Hollow ceramic microspheres (Trelleborg Fillite Inc., Norcross, GA) were used as the starting material. According to the manufacturer, the stock microspheres ranged in size from 5 to 100 μm , and densities ranged from 0.6 to 0.8 $\text{g}\cdot\text{cm}^{-3}$. A stainless steel sieve (opening size 38 μm) and a mesh screen (opening size 30 μm) were used to separate the fraction of microspheres with sizes between 30 and 38 μm . About 2 g of the separated fraction of microspheres were put into Milli-Q water (Millipore Corp. Bedford, MA) to remove whole from broken microspheres by flotation. The floating (intact) microspheres were dried in air, and put into ethyl ether (density 0.71 $\text{g}\cdot\text{cm}^{-3}$) to further narrow the density range. Floating microspheres (density between 0.6 and 0.71 $\text{g}\cdot\text{cm}^{-3}$) were filtered, rinsed with water, and air-dried.

About 0.05 g dried microspheres were spread evenly into an aluminum dish (diameter 2.5 in.) and placed into the vacuum chamber of the Denton Discovery-18 sputtering system (Denton Vacuum, Moorestown, NJ). Prior to sputtering with gold, the glass spheres were sputtered 1 min with chromium at vacuum pressure less than 4×10^{-6} Torr to enhance binding of gold to the microsphere surfaces. Following chromium sputtering, the microspheres were then sputtered with gold (sputtering power 100 w) at a vacuum pressure less than 4×10^{-6} Torr. To produce an even gold coating, gold sputtering was performed in three successive steps of 7.5, 7.5, and 2.5 min, respectively. Between each step, the microspheres were suspended in anhydrous ethanol, filtered, rinsed with Milli-Q water, air-dried, and re-spread into the aluminum dish. The gold and chromium targets were manufactured by Kurt J. Lesker Company (Clairton, PA). Following sputtering, the microspheres were suspended using ethanol, filtered, and rinsed sequentially with Milli-Q water and methanol.

To produce negatively charged hydrophilic surfaces on the microspheres in aqueous solution, the methanol-rinsed gold-coated microspheres were reacted with 10 mL 5 mM mercaptoacetic acid (HSCH_2COOH , Sigma-Aldrich, St. Louis, MO) solution in methanol for at least 24 h. The thiol (SH) group adsorbs covalently onto the gold surface, while the carboxyl group (COOH) extends from the surface into aqueous solution (36–38). In aqueous solution, the carboxyl groups deprotonate, imparting negative charge on microsphere surfaces. Thiol-treated microspheres were dispersible in water, whereas gold-coated microspheres without mercaptoacetic acid treatment floated on the water surface due to their hydrophobicity.

The treated gold-coated microspheres were filtered, rinsed repeatedly with water, and re-suspended into water in a 50 mL centrifuge tube. The fraction of microspheres with a density range between 1.06 and 1.26 $\text{g}\cdot\text{cm}^{-3}$ was separated (for column experiments) based on measured settling velocities. Based on the average density of 1.16 $\text{g}\cdot\text{cm}^{-3}$, the average thickness of the gold layer on the microspheres was 170 nm. Note that sonication was avoided during the entire sputtering, treatment, and separation processes, since sonication was found to cause gold to come off the microspheres.

The concentration of gold-coated microspheres in solution was adjusted to 2.3×10^3 particles $\cdot\text{mL}^{-1}$ for column experiments. This low influent concentration simplified counting of deposited microspheres in reconstructed XMT images, and minimized the potential for aggregation. The pH of the suspension was adjusted to 6.8 using 5×10^{-5} M NaHCO_3 . The suspension was examined using a grooved slide (Hausser Scientific, Horsham, PA) under a microscope. Less than 2% of microspheres were observed as doublets. The average diameter of the gold-coated microspheres was found to be about 36 μm ($35.7 \pm 2.4 \mu\text{m}$).

To check the visibility of the thiol-treated gold-coated microspheres, 0.2 mL of influent microsphere suspension was added into a column (O. D. 10 mm) packed with glass beads (packed length 6 mm). The column was scanned by X-rays and number of microspheres was counted from the reconstructed image. It was found that 90% of microspheres were visible in the XMT images, and this percentage was applied as a correction factor to the concentrations of retained microspheres for mass recovery calculations. The microspheres that were not visible in the reconstructed XMT image presumably had higher initial densities and reduced gold layer thickness relative to the visible microspheres.

Porous Media. The porous media used in the column experiments was 20–25 mesh (average size 780 μm) soda lime glass beads (Cataphote Inc., Jackson, MS) and quartz sand (Fisher Scientific, Fair Lawn, NJ). The glass beads were first rinsed sequentially with acetone and hexane and then soaked with concentrated HCl for 24 h, followed by repeated rinsing with Milli-Q water. The quartz sand was cleaned by soaking in concentrated HCl for at least 24 h, followed by repeated rinsing with ultrapure water, drying at 105 °C and baking overnight at 850 °C. To create favorable deposition conditions, the two porous media (20 cm^3) were soaked in polyethylenimine (Sigma-Aldrich, St. Louis, MO) solution (0.8 g per 100 mL Milli-Q water) for at least 24 h. The treated porous media were air-dried. Adsorption of polyethylenimine to porous media imparts positive charges to porous media grain surfaces.

Column Experiment Conditions. Borosilicate glass columns (75 mm in length and 8 mm in inner diameter) were wet packed with the cleaned porous media to a packed length of 50 mm. Since the sample stage of the XMT facility cannot accommodate samples longer than 40 mm, the glass column consisted of two pieces (each 37 mm long) which can be scanned separately. The two pieces had flanges (2.5 mm thick) at one end to allow connection, which was sealed using Parafilm. Two 60-mesh stainless steel screens (Gerard Daniel Worldwide, Hanover, PA) were placed at the bottom end of the column, and atop the packed porous media, respectively. The porosities of the packed glass beads and quartz sand was 0.404 and 0.376, respectively, as determined by weighing before and after saturating the column and dividing aqueous phase volume (derived from the mass difference) by the total volume of the packed bed.

The packed columns were preequilibrated with about 20 pore volumes of degassed Milli-Q water at a pH of 6.8. One pore volume was equal to 1.01 and 0.94 mL for packed glass beads and quartz sand, respectively. Following preequilibration, 2 pore volumes of the gold-coated microsphere

TABLE 1. Column Experiment Conditions, Mass Recoveries, and Deposition Rate Coefficients Obtained Through Simulation and Theoretical Calculation^a

porous media	fluid velocity (cm·s ⁻¹)	deposition at G–G (%)	single-contact deposition (%)	mass recovery (%)	observed k_f (s ⁻¹)	calculated k_f (s ⁻¹)	
						T–E equation	R–T equation
glass beads	0.10	20.07	79.93	0.83	2.32E–01	1.72×10^{-01}	1.37×10^{-01}
quartz sand	0.10	41.40	58.60	0.96	2.06E–01	2.06×10^{-01}	1.86×10^{-01}
quartz sand	0.25	27.60	72.40	0.67	7.53E–01	2.38×10^{-01}	2.12×10^{-01}

^a G–G represents grain-to-grain contacts. T–E and R–T stand for Tufenkji–Elimelech and Rajagopalan–Tien, respectively.

suspension were introduced in down-flow mode, followed by 3 pore volumes of elution with water at pH of 6.8. During the experiments, the fluid level was maintained at a given distance above the top of the porous media and the columns effluent outlet to ensure a constant pressure head and constant fluid velocity. The transport experiments were carried out at a pore water velocity of 0.1 cm·s⁻¹, with an additional experiment in the quartz sand at 0.25 cm·s⁻¹. These fluid velocity conditions represent engineered riverbank and other filtration systems. The experimental conditions are summarized in Table 1.

The concentrations of the effluent samples were determined by counting microspheres in 25 μL of effluent under a microscope after evaporation of water. For samples having low concentrations, up to 200 μL effluent suspensions of the samples were counted. Following the experiment, the two pieces of the column were separated, sealed at both ends using Parafilm, and scanned by XMT. The porous media remained saturated during scanning. The retained microspheres in the column were counted directly from the reconstructed XMT images. The mass balances were obtained by dividing the total number of microspheres recovered from effluent and retained in the column by the total number of microspheres in the influent.

XMT System and Scanning Procedures. After the column experiments, the two column pieces (with porous media containing microspheres) were scanned using the cone beam XMT system (Konoscope 40–130, Aracor Inc., Sunnyvale, CA) at University of Utah. The Konoscope system was designed and assembled to obtain 2048 × 2048 pixel reconstruction over a 10 mm diameter, while allowing for imaging of somewhat larger samples (40 mm). The device consists of a microfocus X-ray source, a sample positioning stage, and a digital X-ray detection camera. The power of the X-ray source tube was set at 13 W at which the focal spot was 20 μm. A source filter is used to harden the spectrum which reduces beam-hardening artifacts. A computer-controlled vertical/rotary positioning system allowed the sample (column pieces) to rotate 0.72° and move 2.5 μm upward in vertical direction in the X-ray beam. A complete scan consisted of 500 steps, from 0 to 360° and moving 1.25 mm in vertical direction. About 1 h was required to complete a scan and collect 500 projections of the sample. The X-ray detection system consists of a fiberoptic taper, a scintillator/fiberoptic faceplate, and a CCD camera system. The binning factor of CCD camera pixels was set at 4, yielding a spatial resolution of 20 μm. Details of the Konoscope XMT system can be found elsewhere (19).

Each scan produced projection data of packed porous media segments of a length of approximately 8 mm. Since XMT cannot produce all projections for samples with a diameter greater than 10 mm, image reconstruction of the column at the flange connection (5 mm in length) was not possible. Six scans (segments) were required to obtain the projection data for the entire length of the column (45 mm), except the flange connection. The number of deposited microspheres at the connection was interpolated by multiplying the average number deposited in the 3 mm-long

segments above and below the connection by a length correction factor of 1.67 (5 mm/3 mm). The projection data of each segment was used to reconstruct the image of the segment. Reconstruction was done with filtered back-projection algorithm, details of which are provided elsewhere (39).

Medial Axis Analysis. Based on the reconstructed XMT images, the pore spaces were characterized using the medial axis algorithm (3DMA) developed by Lindquist et al. (40). The medial axis is analogous to the skeleton of an object (pore space in this case) running through its geometrical middle. The skeleton preserves the interconnectivity of the pore space. The medial axis is equidistant to at least two neighboring grain surfaces. The sizes of the small medial axis voxels represent the separation distances between the grain surfaces, which may represent pore constrictions or grain-to-grain contacts. The large medial axis voxels represent the sizes of pore bodies. 3DMA generates a size distribution of the medial axis voxels. A larger fraction of small medial axis voxels indicates there are more locations where pore constrictions are narrow and where colloids are more likely to be entrapped physically. More details on medial axis analysis can be found elsewhere (27, 40).

Medial axis analysis of XMT images (resolution 20 μm) yields a minimum medial axis voxel diameter of 40 μm (20 μm to the neighboring grain surfaces from the center of the voxel). Therefore, pore constrictions narrower than 40 μm are all assigned with medial axis voxels of 40 μm. To further characterize the narrow pore constrictions, the XMT images (4.8 mm × 4.8 mm × 4.0 mm) were up-sampled using a 3-dimensional cubic spline algorithm (“unu” from teem software package developed by Gordon Kindlmann at <http://teem.sourceforge.net>), which effectively increases the image resolution to 10 μm through interpolation. Medial axis analysis of the up-sampled images yielded the fraction of medial axis voxels having a diameter of 20 μm.

Results

Representative XMT Images. Representative cross-sectional XMT images of glass bead and quartz sand porous media show porous media grains (gray), pore water (black), and gold-coated hollow microspheres (white) (Figure 1). The grain sizes range from 710 to 850 μm (20–25 mesh); hence, the smaller appearance of some grains or spheres results from their centers being located above or below the particular image plane shown. The quartz grains (Figure 1 right) show greater angularity relative to the glass beads (Figure 1 left), yielding dramatic differences in the length of grain-to-grain contacts in the two porous media. Grain-to-grain contacts that lie within the plane of the image are shown in white boxes (Figure 1). The grain-to-grain contacts in the glass beads have lengths that are a small fraction of the lengths of the grain-to-grain contacts in the quartz sand.

Examination of consecutive cross-sectional images for 50 random grains showed that grains were on average in contact with 6.4 (±1.06) and 7.9 (±1.02) neighboring grains in the glass beads and quartz sand, respectively. For this determination, contact was defined as a grain-to-grain

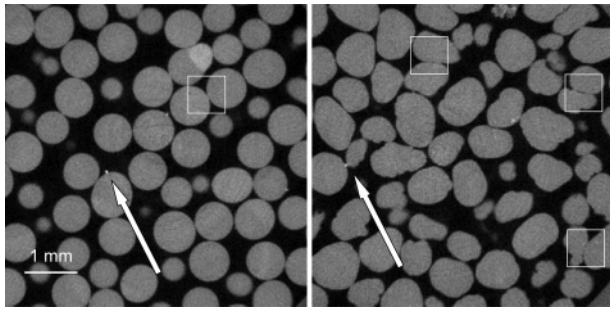


FIGURE 1. Cross-sectional XMT images of porous media: glass beads (left) and quartz sand (right). Gray areas represent porous media grains. Black areas represent pore spaces saturated with solution. White spots (pointed by arrows) are gold-coated microspheres. Shown in white boxes are grain-to-grain contacts that are in the image plane.

separation distance less than the scanning resolution used (20 μm). The average number of contacts converged to the above values when the numbers of randomly picked grains exceeded 30.

Figure 1 demonstrates a large distribution in separation distance between grains ranging from zero to over 300 μm . In contrast, the Happel sphere-in-cell model (2, 5) idealizes this distribution of separation distances as single uniform separation distance. The idealized thickness of the uniform fluid shell (s) surrounding the grains is as follows:

$$s = [(1 - \theta)^{-1/3} - 1]R_c$$

where θ is the porosity of the porous media, and R_c is the radius of the grain (collector). In the glass beads, $\theta = 0.4$ and $R_c = 390 \mu\text{m}$, yielding $s = 72 \mu\text{m}$, which translates to a calculated 144 μm separation distance between the grains, which is an average of the distribution indicated by Figure 1.

Some deposited microspheres contact two grains (deposition at grain-to-grain contacts) (Figure 1 right), whereas others contact only one grain (single-contact deposition) (Figure 1 left). Microsphere deposition at wall-to-grain contacts was considered equivalent to deposition at grain-to-grain contacts, and comprised between 10 and 20% of grain-to-grain contact deposition. In both porous media, no microsphere was observed to contact simultaneously with three grains, indicating that deposition at grain-to-grain contacts observed here is not necessarily equivalent to straining, which has been defined as physical entrapment in pore constrictions too small to pass (41). Examination of consecutive cross-sectional images yielded the numbers of microspheres deposited at grain-to-grain contacts and at single-contact areas.

Deposition at Grain-to-Grain Contacts. In the glass bead and quartz sand porous media, all injected microspheres were deposited under the conditions examined (absence of an energy barrier), i.e., breakthrough and elution concentrations were equal to zero. Mass recoveries $>83\%$ were achieved for experiments at a pore water velocity of 0.1 $\text{cm}\cdot\text{s}^{-1}$ for both porous media (Table 1), which are quite reasonable considering that the enumeration of aqueous samples was subject to a standard error of about 10%. However, for one experiment (quartz sand at a pore water velocity of 0.25 $\text{cm}\cdot\text{s}^{-1}$) the mass recovery was relatively low (67%), and this is unexplained.

Deposition at grain-to-grain contacts in the absence of an energy barrier comprised 20.1% of deposition in the glass beads and 41.4% of deposition in the quartz sand, at the fluid velocity of 0.1 $\text{cm}\cdot\text{s}^{-1}$ (Table 1 and Figure 2). Since all introduced microspheres were deposited, the percents

deposited relative to total deposited and total introduced were equivalent.

An increase in the pore water velocity from 0.1 to 0.25 $\text{cm}\cdot\text{s}^{-1}$ in quartz sand yielded a decrease in the percent deposited at grain-to-grain contacts from 41.4% to 27.6%, respectively. For both fluid velocities, the same numbers of microspheres were introduced, and all were deposited. Hence, this mild change may indicate that a smaller fraction of colloid trajectories intercepted grain-to-grain contacts as fluid velocity increased. Since the existence of grain-to-grain contacts is prerequisite to straining, the observation also indicates that the threshold diameter ratio for straining may depend on fluid velocity.

Retained Profiles and Deposition Rate Coefficients. The concentrations of deposited microspheres decreased log-linearly with distance from the source in both the glass bead and quartz sand porous media (Figures 2 and 3). In these figures, each data point represents the number of deposited microspheres in a 0.5-cm segment of porous media; the lines, therefore, represent trends rather than concentrations. Remarkably, the number of microspheres deposited at grain-to-grain contacts also decreased log-linearly with distance from the source, parallel to the profiles for total deposition.

Deposition rate coefficients (k_f) were determined from the retained colloid concentrations as follows:

$$S(x) = \frac{t_o \theta k_f C_o}{\rho_b} \exp\left[-\frac{k_f}{v}x\right]$$

where x is the distance from the inlet, t_o is the injection duration, C_o is the influent concentration (2.3×10^3 particles- cm^{-3}), ρ_b is the bulk porous media density ($2.65 \text{ g}\cdot\text{cm}^{-3}$), v is the pore water velocity. For this calculation, the mass recovery for each experiment was adjusted to 100% by multiplying the numbers of microspheres retained in all segments by a single factor. Taking the natural log of both sides of the above equation yields

$$\ln[S(x)] = \ln\left(\frac{t_o \theta k_f C_o}{\rho_b}\right) - \frac{k_f}{v}x$$

which allows k_f to be determined from the slope of the modified profile of retained microspheres.

Deposition rate coefficients obtained using this approach were 0.23 and 0.21 s^{-1} in the glass beads and quartz sand, respectively (pore water velocity = 0.1 $\text{cm}\cdot\text{s}^{-1}$) (Table 1). The deposition rate coefficient increased (from 0.21 to 0.75 s^{-1}) with increasing fluid velocity (from 0.1 to 0.25 $\text{cm}\cdot\text{s}^{-1}$) in quartz sand.

Distributions of Medial Axis Voxel Diameters. Histograms of the medial axis voxel diameters reveal that in both porous media, a significant fraction of voxel diameters were less than 40 μm (Figure 4), representing locations where the 36- μm microspheres can deposit in simultaneous contact with two separate grain surfaces. The fraction of small medial axis voxels ($<40 \mu\text{m}$) was about a factor of 2 greater in quartz sand (20.5%) relative to the glass beads (11.6%) (Figure 4), consistent with the observed a factor of 2 greater deposition at grain-to-grain contacts in the quartz sand (41.4%) relative to the glass beads (20.1%) at same fluid velocity (0.1 $\text{cm}\cdot\text{s}^{-1}$). Note that the voxel diameters do not necessarily represent pore constrictions. Rather, a series of $<40 \mu\text{m}$ voxels may exist along each grain-to-grain contact, and the larger number of these voxels in quartz sand results from the greater average number of contacts with neighboring grains, and greater average grain-to-grain contact length relative to the glass beads.

Discussion

Influence of Grain-to-Grain Contacts in the Absence of an Energy Barrier. Filtration theory idealizes the porous media

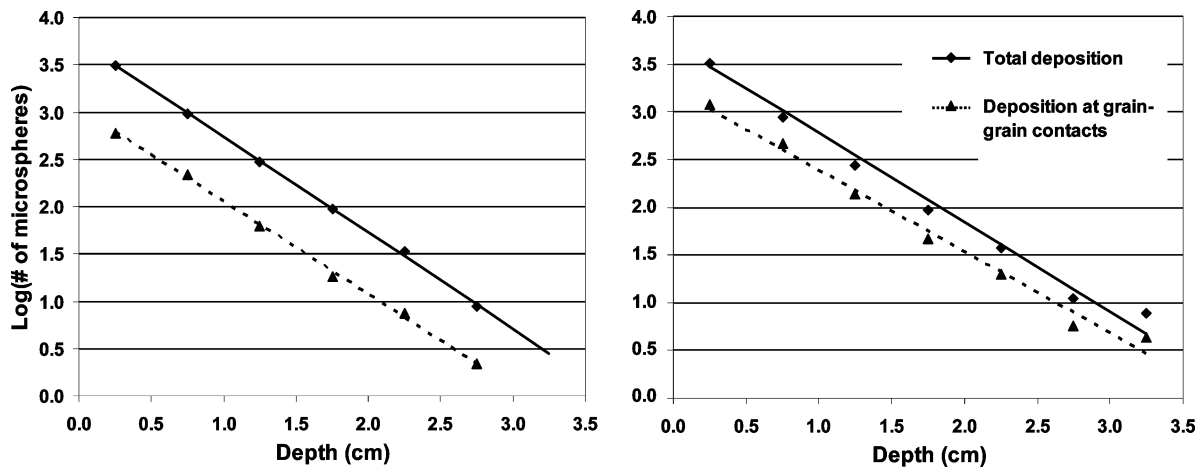


FIGURE 2. Profiles of total deposition and deposition at grain-to-grain contacts in glass beads (left) and quartz sand (right) at a pore water velocity of 0.1 cm-s^{-1} . No deposition was observed at transport distances greater than 3 and 3.5 cm in glass beads and quartz sand, respectively. Depositions at grain-grain contacts account for 20.1% and 41.4% of total depositions in glass beads and quartz sand, respectively.

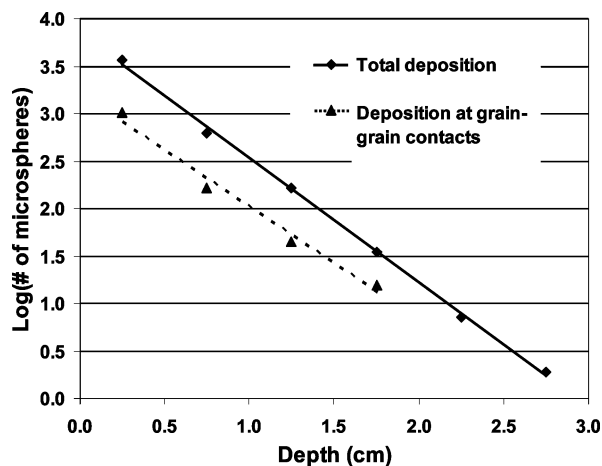


FIGURE 3. Profiles of total deposition and deposition at grain-to-grain contacts in quartz sand at a pore water velocity of 0.25 cm-s^{-1} . Deposition at grain-to-grain contacts and single-contact deposition was observed at transport distances up to 2 and 3 cm, respectively. Deposition at grain-to-grain contacts accounted for 27.6% of total deposition.

as a collection of spherical grains that are completely surrounded by fluid envelopes; whereas the packed structure in an actual porous media is supported via grain-to-grain contacts, and grains cannot, in reality, be completely surrounded by fluid. Despite this idealization, filtration theory clearly provides an excellent approximation of the deposition process in the absence of an energy barrier to deposition (e.g., refs 42 and 43).

Values of k_f determined from experiments for the $36\text{-}\mu\text{m}$ microspheres can be compared with expectations from filtration theory based on following equation:

$$k_f = \frac{3}{2} \frac{(1 - \theta)}{d_c} v \alpha \eta$$

where v is the fluid velocity, d_c is the grain diameter, and α is the collision efficiency (set to unity in the absence of a barrier to deposition), and the single collector efficiency (η) can be calculated using the correlation equations developed by Rajagopalan and Tien (2) and Tufenkji and Elimelech (3), respectively. Combined Hamaker constants of $4.63 \times 10^{-20} \text{ J}$ and $2.62 \times 10^{-20} \text{ J}$ were used in the correlation equations for the quartz-water-gold system and the glass-water-

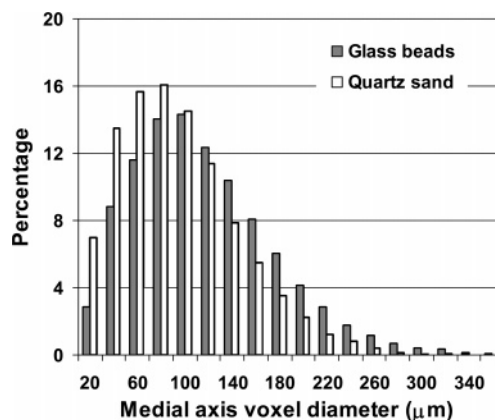


FIGURE 4. Distributions of medial axis voxel diameters in glass beads and quartz sand. The diameters of small medial axis voxels represent the separation distances of pore constrictions. The greater fraction of small medial axis voxel diameters indicates more locations where the pore constrictions are narrow.

gold system, respectively. These combined Hamaker constants were derived from the corresponding individual constants: $3.74 \times 10^{-20} \text{ J}$ for water (44), $6.34 \times 10^{-20} \text{ J}$ for glass (44), $8.86 \times 10^{-20} \text{ J}$ for quartz (45), and $4.0 \times 10^{-19} \text{ J}$ for gold (46). The calculated deposition rate coefficients (Table 1) agree well (within a factor of 1.5) with experimental values except for the quartz sand at a pore water velocity of 0.25 cm-s^{-1} , where the observed value was about a factor of 3.3 greater than the calculated value. Observed deposition rate coefficients increased with fluid velocity, also consistent with predictions by filtration theory in the absence of an energy barrier (Table 1).

The location of deposition on grain surfaces with respect to forward versus rear stagnation points on media grains also displays consistency with filtration theory. The particle trajectory simulations used to develop filtration theory oriented flow in the same direction as gravity. Under this condition deposition is enhanced at forward stagnation points where gravity enhances colloid flux toward the surface. In contrast, gravity would reduce colloid flux toward rear stagnation surfaces. This effect was observed in our experiments, which were conducted with downward flow. Single-contact deposition was dominantly on forward stagnation points (80% of single-contact deposition), in agreement with theory.

Deposition at grain-to-grain contacts comprised a significant portion of overall deposition, about 40% and 20% in the quartz sand and glass beads, respectively, reflecting the difference between idealized and actual fluid trajectories due to grain-to-grain contacts. The trajectory model by Cushing and Lawler (6) demonstrated that inclusion of grain-to-grain contacts in the pore geometry produced significant deposition at these contacts. The observation of log-linear profiles for colloids retained at grain-to-grain contacts in the absence of an energy barrier to deposition indicates that deposition under these conditions is consistent with physicochemical filtration, that is, it is reasonable to conclude that the colloids were retained at the location of collision with the collector surface. Our results demonstrate that, in the absence of an energy barrier, a significant fraction of colloid deposition occurs at grain-to-grain contacts; whereas colloid deposition is well-predicted by a model that neglects the existence of grain-to-grain contacts. This indicates that although grain-to-grain contacts alter the environment of deposition, they do not (in the absence of an energy barrier) significantly influence the probability of collision with the collector surface. This is in stark contrast to the role of grain-to-grain contacts in deposition in the presence of an energy barrier, as demonstrated in the companion paper (44). In the presence of an energy barrier, colloid deposition occurs dominantly at grain-to-grain contacts, and the magnitudes and shapes of the retained profiles deviate drastically from expectations from filtration theory (44).

Relevance to Smaller Colloids. The relatively large size of the colloids used here (36 μm) may render the observed results inapplicable to smaller colloids (despite the fact that these large colloids are near neutrally buoyant) since fluid drag is greater for larger colloids. However, the log-linearity of the observed profile of retained colloid concentrations with distance from source, and the close agreement of observed deposition rate coefficients with expectations from filtration theory, argue strongly that the physicochemical processes governing deposition of these larger colloids are equivalent to those governing deposition of smaller colloids. Furthermore, in a companion paper (47) we demonstrate that in the presence of an energy barrier to deposition the profiles of retained particles deviate from log-linearity similarly to those that have been observed for smaller colloids, e.g., for 1.1- μm colloids as described by Li and Johnson (43) and Tong et al. (48).

Acknowledgments

This material is based upon work supported by the National Science Foundation Hydrologic Sciences Program (EAR 0337258). Any opinions, findings, and conclusions or recommendations expressed in this material are those of the author(s) and do not necessarily reflect the views of the National Science Foundation. X.L. wishes to thank Minjian Yu at the Department of Family and Consumer Studies of the University of Utah for her help with the column experiments. The authors wish to thank two anonymous reviewers for their helpful comments.

Literature Cited

- (1) Yao, K. M.; Habibian, M. T.; O'Melia, C. R. Water and waste water filtration: Concepts and applications. *Environ. Sci. Technol.* **1971**, *5*(11), 1105–1112.
- (2) Rajagopalan, R.; Tien, C.; Trajectory analysis of deep-bed filtration with the sphere-in-cell porous media model. *AIChE J.* **1976**, *22*, 2(3), 523–533.
- (3) Tufenkji, N.; Elimelech, M. Correlation equation for predicting single-collector efficiency in physicochemical filtration in saturated porous media. *Environ. Sci. Technol.* **2004**, *38*, 529–536.
- (4) Nelson, K. E.; Ginn, T. R. Colloid filtration theory and the Happel sphere-in-cell model revisited with direct numerical simulation of colloids. *Langmuir* **2005**, *21*(6), 2173–2184.

- (5) Happel, J. Viscous flow in multiparticle systems: slow motion of fluids relative to beds of spherical particles. *AIChE J.* **1958**, *4*(2), 197–201.
- (6) Cushing, R. S.; Lawler, D. F. Depth filtration: fundamental investigation through three-dimensional trajectory. *Environ. Sci. Technol.* **1998**, *32*, 3793–3801.
- (7) Elimelech, M.; O'Melia, C. R. Kinetics of deposition of colloidal particles in porous media. *Environ. Sci. Technol.* **1990**, *24*(10), 1528–1536.
- (8) Bradford, S. A.; Yates, S. R.; Bettahar, M.; Simunek, J. Physical factors affecting the transport and fate of colloids in saturated porous media. *Water Resour. Res.* **2002**, *38*(12), 1327–1338.
- (9) Sakthivadivel, R. *Theory and mechanism of filtration of non-colloidal fines through a porous medium*, Report HEL 15–5; Hydraulic Engineering Laboratory, University of California: Berkeley, 1966.
- (10) Sakthivadivel, R. *Clogging of a granular porous medium by sediment*, Report HEL 15–7; Hydraulic Engineering Laboratory, University of California: Berkeley, 1969.
- (11) Bradford, S. A.; m. B. M.; Simunek, J.; van Genuchten, M. Th. Straining and attachment of colloids in physically heterogeneous porous media. *Vadose Zone J.* **2004**, *3*, 384–394.
- (12) Crist, J. T.; McCarthy, J. F.; Zevi, Y.; Baveye, P.; Throop, J. A.; Steenhuis, T. S. Pore-scale visualization of colloid transport and retention in partly saturated porous media. *Vadose Zone J.* **2004**, *3*, 444–450.
- (13) Crist, J. T.; Zevi, Y.; McCarthy, J. F.; Throop, J. A.; Steenhuis, T. S. Transport and retention mechanisms of colloids in partially saturated porous media. *Vadose Zone J.* **2005**, *4*, 184–195.
- (14) Bradford, S. A.; Simunek, J.; Bettahar, M.; Tadassa, Y. F.; van Genuchten, M. T.; Yates, S. R. Straining of colloids at textural interfaces. *Water. Resour. Res.* **2005**, *41*, doi: 10.1029/2004WR003675.
- (15) Olson, M. S.; Ford, R. M.; Smith, J. A.; Fernandez, E. J. Quantification of bacterial chemotaxis in porous media using magnetic resonance imaging. *Environ. Sci. Technol.* **2004**, *38*(14), 3864–3870.
- (16) Olson, M. S.; Ford, R. M.; Smith, J. A.; Fernandez, E. J. Analysis of column tortuosity for MnCl_2 and bacterial diffusion using magnetic resonance imaging. *Environ. Sci. Technol.* **2005**, *39*(1), 149–154.
- (17) Baumann, T.; Werth, C. J. Visualization of colloid transport through heterogeneous porous media using magnetic resonance imaging. *Colloid Surf., A* **2005**, *265*, 2–10.
- (18) Rivers, M. L. Tutorial introduction to X-ray computed microtomography data processing. Available at <http://www-fp.mcs.anl.gov/xray-cmt/rivers/tutorial.html>. **1998**.
- (19) Lin, C. L.; Miller, J. D.; Cone beam X-ray microtomography—A new facility for 3D analysis of multiphase materials. *Miner. Metall. Process.* **2002**, *19*(2), 65–71.
- (20) Wildenschild, D.; Hopmans, J.; Vaz, C.; Rivers, M.; Rikard, D.; Christensen, B. Using X-ray computed tomography in hydrology: systems, resolutions, and limitations. *J. Hydrol.* **2002**, *267*(3–4), 285–297.
- (21) Coker, D. A.; Torquato, S. Morphology and physical properties of Fontainebleau sandstone via a tomographic analysis. *J. Geophys. Res.* **1996**, *101*(B8), 17497–17506.
- (22) Auzeais, F. M.; Dunsmuir, J.; Ferreol, B. B.; Martys, N.; Olson, J.; Ramakrishnan, T. S.; Rothman, D. H.; Schwartz, L. M. Transport in sandstone: a study based on three-dimensional microtomography. *Geophys. Res. Lett.* **1996**, *23*(7), 705–708.
- (23) Coles, M. E.; Hazlett, R. D.; Muegge, E. L.; Jones, K. W.; Andrews, B.; Dowd, B.; Siddons, P.; Peskin, A.; Spanne, P.; Soll, W. Developments in synchrotron X-ray microtomography with applications to flow in porous media. *SPE Reservoir. Eval. Eng.* **1998**, *1*(4), 288–296.
- (24) Coles, M. E.; Hazlett, R. D.; Spanne, P.; Soll, W. E.; Muegge, E. L.; Jones, K. W. Pore level imaging of fluid transport using synchrotron X-ray microtomography. *J. Pet. Sci. Eng.* **1998**, *19*(1–2), 55–63.
- (25) Schwartz, L. M.; Auzeais, F.; Dunsmoir, J.; Martys, N.; Bentz, D. P.; Torquato, S. Transport and diffusion in three-dimensional composite media. *Physica, A* **1994**, *207*, 28–36.
- (26) Spanne, P.; Thovert, J. F.; Jacquin, C. J.; Lindquist, W. B.; Jones, K. W.; Adler, P. M. Synchrotron computed microtomography of porous media: topology and transports. *Phys. Rev. Lett.* **1994**, *73*(14), 2001–2004.
- (27) Lin, C. L.; Miller, J. D. Pore structure analysis of particle beds for fluid transport simulation during filtration. *Int. J. Miner. Process.* **2004**, *73*, 281–294.
- (28) Al-Raoush, R. I.; Willson, C. S. Extraction of physically realistic pore network properties from three-dimensional synchrotron

- X-ray microtomography images of unconsolidated porous media systems. *J. Hydrol.* **2005**, *300*, 44–64.
- (29) Wildenschild, D. J.; Hopmans, W.; Rivers, M. L.; Kent, A. J. R. Quantitative analysis of flow processes in a sand using synchrotron-based X-ray microtomography. *Vadose Zone J.* **2005**, *4*, 112–126.
- (30) Al-Raoush, R. I.; Willson, C. S., A pore-scale investigation of a multiphase porous media system. *J. Contam. Hydrol.* **2005**, *77*, 67–89.
- (31) Bentz, D. P.; Quenard, D. A.; Kunzel, H. M.; Baruchel, J.; Peyrin, F.; Martys, N. S.; Garboczi, E. J. Microstructure and transport properties of porous building materials: II. Three-dimensional X-ray tomographic studies. *Mater. Struct.* **2000**, *33*(227), 147–153.
- (32) Altman, S. J.; Peplinski, W. J.; Rivers, M. L. Evaluation of synchrotron X-ray computerized microtomography for the visualization of transport processes in low-porosity materials. *J. Contam. Hydrol.* **2005**, *78*, 167–183.
- (33) Hazlett, R. D. Simulation of capillary-dominated displacements in microtomographic images of reservoir rocks. *Transp. Porous Media* **1995**, *20*(1–2), 21–35.
- (34) Olson, J. F.; Rothman, D. H. Two-fluid flow in sedimentary rock: simulation, transport and complexity. *J. Fluid Mech.* **1997**, *341*, 343–370.
- (35) Nakashima, Y.; Nakano, T.; Nakamura, K.; Uesugi, K.; Tsuchiyama, A.; Ikeda, S. Three-dimensional diffusion of non-sorbing species in porous sandstone: computer simulation based on X-ray microtomography using synchrotron radiation. *J. Contam. Hydrol.* **2004**, *74*, 253–264.
- (36) Chung, C. L. M. Self-assembled monolayers of mercaptoacetic acid on Ag powder: characterization by FT-IR diffuse reflection spectroscopy. *Bull. Korean Chem. Soc.* **2004**, *25*(10), 1461–1462.
- (37) Ederth, T.; Claesson, P.; Liedberg, B. Self-assembled monolayers of alkanethiolates on thin gold films as substrates for surface force measurements. Long-range hydrophobic interactions and electrostatic double-layer interactions. *Langmuir* **1998**, *14*, 4782–4789.
- (38) Drellich, J.; Wilbur, J. L.; Miller, J. D.; Whitesides, G. M. Contact angles for liquid drops at a model heterogeneous surface consisting of alternating and parallel hydrophobic/hydrophilic strips. *Langmuir* **1996**, *12*, 1913–1922.
- (39) Feldcamp, L. A.; Davis, L. C.; Kress, J. W. Practical cone-beam algorithm. *J. Opt. Soc. Am.* **1984**, *1*(6), 612–619.
- (40) Lindquist, W. B.; Lee, S.; Coker, D. A.; Jones, K. W.; Spanne, P. Medial axis analysis of void structure in three-dimensional tomographic images of porous media. *J. Geophys. Res.* **1996**, *101*(B4), 8297–8310.
- (41) Herzig, J. P.; Leclerc, D. M.; LeGoff, P. Flow of suspensions through porous media: application to deep filtration. *Ind. Eng. Chem.* **1970**, *62*, 8–35.
- (42) Li, X.; Scheibe, T. D.; Johnson, W. P. Apparent decreases in colloid deposition rate coefficient with distance of transport under unfavorable deposition conditions: a general phenomenon. *Environ. Sci. Technol.* **2004**, *38*(21), 5616–5625.
- (43) Li, X.; Johnson, W. P. Nonmonotonic variations in deposition rate coefficients of microspheres in porous media under unfavorable deposition conditions. *Environ. Sci. Technol.* **2005**, *39*(6), 1658–1665.
- (44) Bergendahl, J.; Grasso, D. Prediction of colloidal detachment in a model porous media: thermodynamics. *AIChEJ* **1999**, *45*(3), 475–484.
- (45) Bergstrom, L. Hamaker constants of inorganic materials. *Adv. Colloid Interface Sci.* **1997**, *70*, 125–169.
- (46) Adamson, A. W. *Physical Chemistry of Surfaces*, 5th ed.; Wiley: New York and London, 1990.
- (47) Li, X.; Lin, C. L.; Miller, J.; Johnson, W. P. Role of grain-to-grain contacts on profiles of retained colloids in porous media in the presence of an energy barrier to deposition. *Environ. Sci. Technol.* **2006**, *40*, *****.
- (48) Tong, M.; Li, X.; Brow, C.; Johnson, W. P. Detachment-influenced transport of an adhesion-deficient bacterial strain within water-reactive porous media. *Environ. Sci. Technol.* **2005**, *39*(8), 2500–2508.

Received for review December 13, 2005. Revised manuscript received April 10, 2006. Accepted April 13, 2006.

ES0525004